Chemical Science

ROYAL SOCIETY OF CHEMISTRY

EDGE ARTICLE

View Article Online
View Journal | View Issue

Cite this: *Chem. Sci.*, 2026, **17**, 5092

All publication charges for this article have been paid for by the Royal Society of Chemistry

Sulfone-functionalized stereoisomeric [3]radialene displays guest induced modulation of porous frameworks and critical crystallization-induced near-infrared emission

Gaoqiang Xu,[ab] Ying Zhao,[a] Sheng Xie, *[ac] Zhibiao Zhou,[ad] Ziyu Luo,[e] Haohao Liu,[a] Yang Zhang,[a] Zijie Qiu, [b] Anlian Pan, *[e] Zebing Zeng *[a] and Ben Zhong Tang *[b]

Luminescence-responsive porous organic materials have garnered significant interest due to their chemical versatility, adaptability and potential applications in smart sensors and optoelectronic devices. In this study, we introduce a novel class of sulfone-functionalized stereoisomeric [3]radialenes **TTRO** with quasi-C_3 symmetry, which demonstrate flexible structural configurations and the ability to form diverse crystalline frameworks with tunable porosity ranging from 0% to 31.2%. These assembled frameworks are characterized by distinct stereochemical configurations of **TTRO**, which influence their dipole moment vectors and molecular packing parameters, especially the geometry of the *exo*-cyclic radialene ring. The stability of these structures is further enhanced by sulfone-embedded aromatics and guest solvent molecules, establishing a network of multivalent molecular interactions. Remarkably, **TTRO**-based materials exhibit crystallization-induced emission in the near-infrared (NIR) region (650–1000 nm), transitioning from non-emissive amorphous powders to exhibiting strong photoluminescence (up to 24.1%) in guest-involved porous crystalline frameworks. Time-resolved fluorescence and computational analyses reveal that the dynamic stacking geometry of **TTRO** units, combined with multivalent sulfone-based intermolecular interactions with guest molecules, modulates the reorganization energy within the frameworks, thereby tuning solid-state emission. These findings provide new insights and strategies for designing NIR luminophores through crystalline engineering of [3]radialene materials.

Received 8th September 2025
Accepted 7th January 2026

DOI: 10.1039/d5sc06925d

rsc.li/chemical-science

Introduction

The peculiar [3]radialenes exhibit a planar-centered, radiating topology of cross-conjugated *exo*-double bonds, representing a distinctive molecular scaffold within organic materials.[1–9] The bare [3]radialene, being a structural isomer of benzene, is inherently susceptible to olefinic polymerisation.[3] Chemical modification of the exocyclic C=C bond using sterically protective groups is typically necessary to improve thermal and kinetic stability for practical applications.[10,11] The synthesis and derivation of these compounds remain challenging due to the construction of the three-membered radialene ring. These exocyclic, extended [3]radialenes exhibit a variety of remarkable characteristics, including multi-step redox behaviors, efficiency as organic *P*-dopants in semiconductors,[7,12–15] and unique photon absorption/emission properties.[16–18] In particular, the simple hexaphenyl[3]radialene exhibits light absorption in the blue region (465 nm) and strong emission in the long-wavelength region (618 nm), with a large Stokes shift beyond 150 nm.[19,20] Furthermore, the electron-donating and -accepting substitutions tune the optoelectronic behaviors in different physical states.[12–15,21] These features are primarily attributed to the cross-conjugated electron-π system with a narrow energy gap and special vibrational dynamics in the excited states, but the underlying processes have not been extensively studied.[6,18,22]

In addition to their distinctive optical properties, these planar [3]radialenes adopt a quasi C_3 symmetric system at their periphery, providing versatile yet rare building blocks for functional molecular materials.[23–26] These [3]radialene

[a]*State Key Laboratory of Chemo and Biosensing, College of Chemistry and Chemical Engineering, Hunan University, Changsha 410082, China. E-mail: shengxie@hnu.edu.cn; zbzeng@hnu.edu.cn*

[b]*Guangdong Basic Research Centre of Excellence for Aggregate Science, School of Science and Engineering, Shenzhen Institute of Aggregate Science and Technology, The Chinese University of Hong Kong, Shenzhen (CUHK-Shenzhen), Guangdong 518172, China. E-mail: tangbenz@cuhk.edu.cn*

[c]*Shenzhen Research Institute, Hunan University, Shenzhen 518000, China*

[d]*TCM and Ethnomedicine Innovation and Development International Laboratory, Innovative Materia Medica Research Institute, School of Pharmacy, Hunan University of Chinese Medicine, Changsha, China*

[e]*Hunan Institute of Optoelectronic Integration, College of Materials Science and Engineering, Hunan University, Changsha 410082, China. E-mail: anlian.pan@hnu.edu.cn*

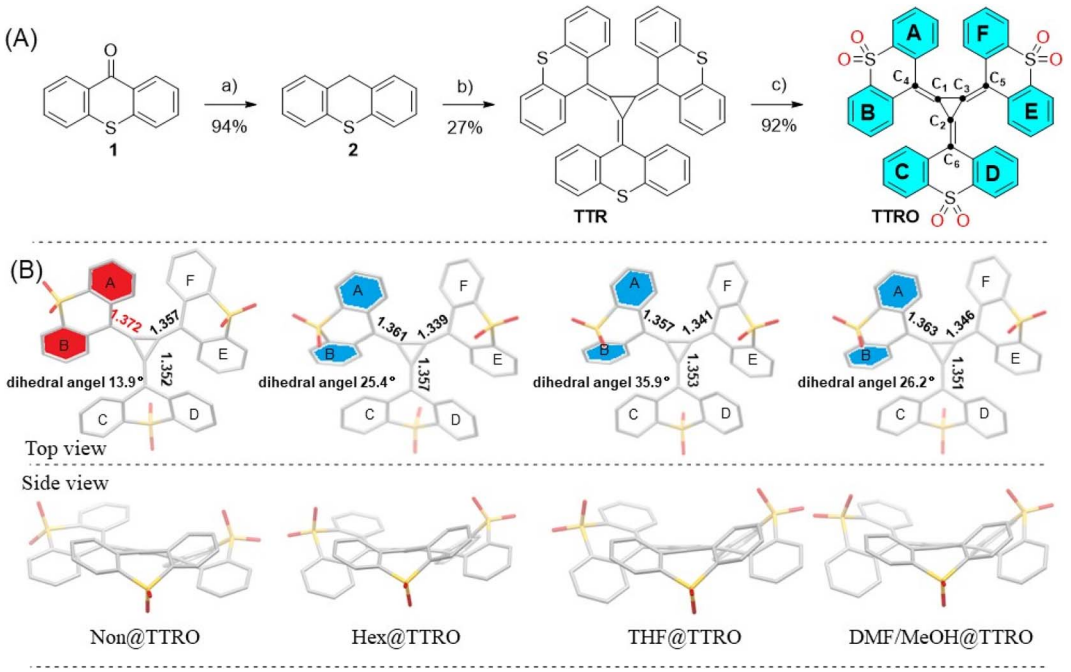

Fig. 1 (A) Synthesis of sulfone[3]radialene (**TTRO**). Conditions: a) $NaBH_4$, I_2, THF, 0 °C to 65 °C, 12 h. b) i. *n*-BuLi, THF/DMSO (v/v = 1 : 1), 0 °C to rt, 1 h; ii. Tetrachlorocyclopropene (**TCCP**), 0 °C to rt, 1 h; iii. Bubbling O_2, 0 °C to rt, 1 h. c) *m*-chloroperoxybenzoic acid, DCM, rt, 12 h. (B) Crystal structures of **TTRO** in different crystalline frameworks with highlighted bonds and dihedral angles.

substituents convey a propeller conformation due to steric hindrance along the central ring. Cross-coupling of these substituents within the [3]radialene scaffold can produce diverse porous frameworks with unique topologies. Interestingly, our earlier report revealed that the assembly of stereoisomeric *α*-cyano triaryl[3]radialene exhibited tight stacking through CN-mediated supramolecular coupling interactions.[6] This resulted in the clustering-enhanced excimer emission of radialene molecules at the mesoscale, albeit with concentration-caused quenching of the dispersed single molecules.[6] Hence, exploring [3]radialenes as a functional building block could improve our fundamental understanding of topological conjugation effects.

In this study, we report the synthesis and characterization of sulfone-functionalized stereoisomeric [3]radialene **TTRO**, obtained through the oxidation of trithioxanthene[3]radialene **TTR** (Fig. 1). Although the molecular formula shows three identical fragments, the overcrowded radialene system produces distinctive asymmetrical features in the aromatic substituents (Fig. 1B, right). Rings E and F in one wing are highly twisted (*i.e.*, not coplanar), while the other two wings (A/B and C/D) are freely stretched (*i.e.*, close to coplanar). Furthermore, these asymmetrical stereo configurations can be modulated by guest solvent molecules, yielding different crystalline porous frameworks that exhibit the critical phenomenon of crystallization-induced NIR emission. We characterized four different crystalline structures and the photophysical properties of the same **TTRO**, paying particular attention to the solid-state configurational changes of the radialene rings. Experimental and computational studies suggest that the electron-withdrawing sulfone group plays a key role in the formation of these diverse crystalline frameworks *via* d–p π bonding interactions in the ground state.[27–30] The multivalent interactions of the sulfone group adjust the stretching vibration of *exo*-double bonds in the [3]radialene ring, which are intuitively important for triggering crystalline photoluminescence.[28–31]

Results and discussion

Preparation of sulfone[3]radialene

Trithioxanthene[3]radialene (**TTR**) was synthesized by following a modified Fukunaga's method, which involves reacting stabilized carbanions with tetrachlorocyclopropene (**TCCP**) (Fig. 1A).[32,33] Thioxanthene (**2**) was first deprotonated using *n*-BuLi in a dry tetrahydrofuran (THF)/DMSO solution at 0 °C. This was followed by treatment with **TCCP** in a manifold nucleophilic substitution reaction. The resulting dark red solution was then oxidized with oxygen to produce **TTR** as blue purple solids in a 27% yield. Subsequently, **TTR** was oxidized with *m*-chloroperoxybenzoic acid to provide sulfone[3]radialene (**TTRO**) as reddish-brown solids in a 92% yield. Their chemical structures were characterized using nuclear magnetic resonance (Fig. S1–S4) and high-resolution mass spectrometry (Fig. S5 and S6) and were further confirmed by X-ray crystallography analysis (Fig. 1B, and Tables S1–S5). These [3]radialenes have good chemical and thermal stability under mild conditions. Diverse **TTRO** crystals can be obtained through laboratory crystallization processes involving the diffusion of a poor solvent into a **TTRO** solution (Fig. 1B). **Hex@TTRO** single crystals are obtained from $CHCl_3$/hexane with hexane included; **THF@TTRO** from THF/cyclohexane with THF included; **Non@TTRO** without solvent inclusion; and **DMF/MeOH@TTRO**

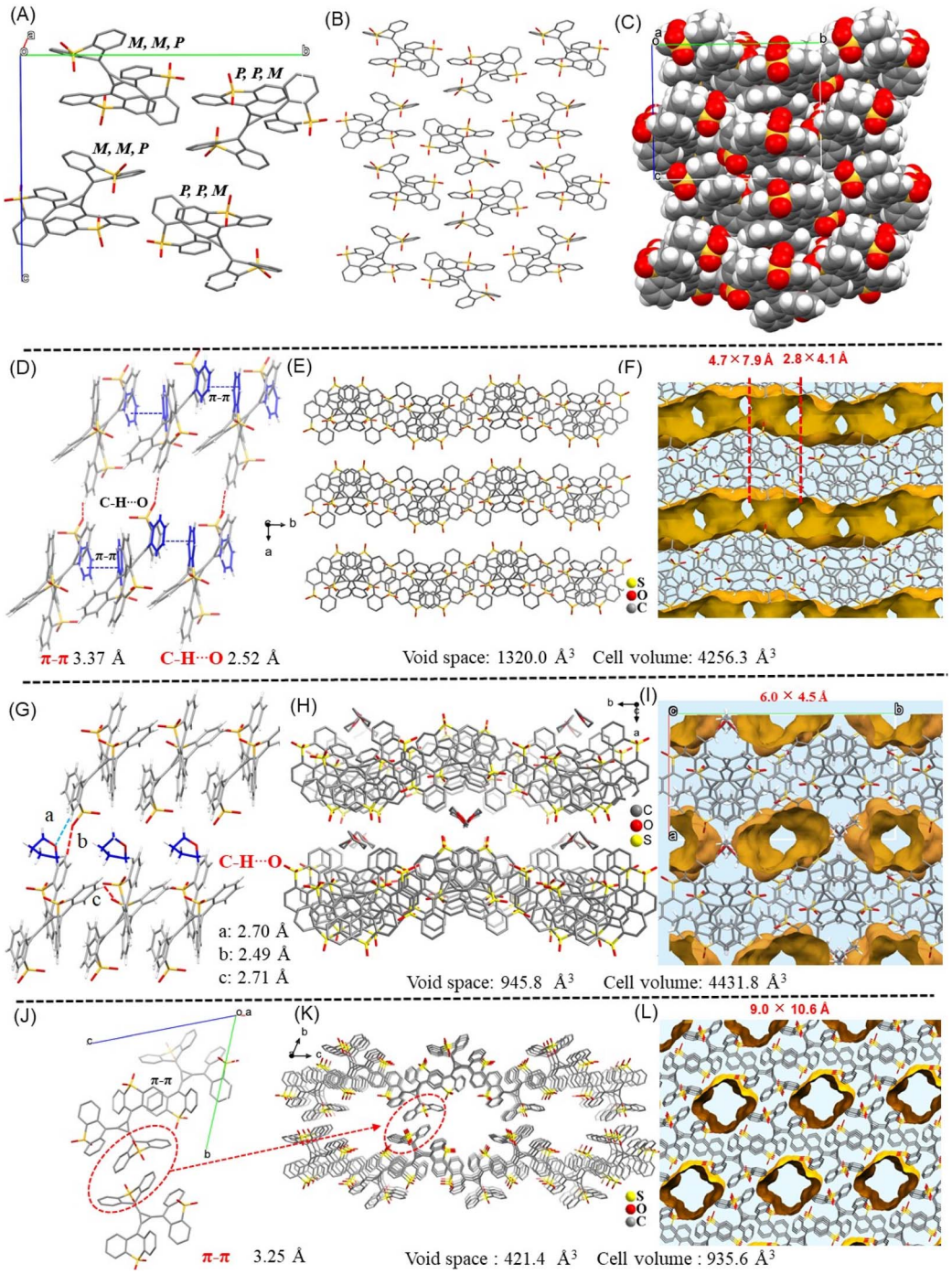

Fig. 2 X-ray single-crystal structures, the intermolecular interactions and 3D molecular packing structure and void spaces of porous crystalline frameworks of (A–C) **Non@TTRO**, (D–F) **Hex@TTRO**, (G–I) **THF@TTRO**, and (J–L) **DMF/MeOH@TTRO**.

from DMF/MeOH with DMF and MeOH included. Solvent molecules typically fill the spaces between layers in a stacked structure of single crystals, and most of these crystals are fairly stable. The stability of the resulting crystal structure depends on intermolecular forces, which vary according to the configuration of the individual molecules and the solvent molecules filling the crystals. Thermogravimetric analysis (TGA) of polycrystalline **Hex@TTRO** solids reveals minimal weight loss up to 300 °C, with approximately 50% weight loss observed when heated to 800 °C. This suggests that **Hex@TTRO** crystalline samples possess excellent thermal stability (Fig. S7). In contrast, **THF@TTRO** crystals are relatively unstable and undergo slow weathering in an air atmosphere.

Modulable stereo-configuration in crystalline states

As expected, the NMR spectra of **TTR** and **TTRO** in $CDCl_3$ showed well-resolved and identical signals for all the peripheral phenyl rings, suggesting a certain degree of symmetry in the

solution state (Fig. S1–S4).[34] However, the X-ray crystalline structures obtained show that the radialene exhibits modulable asymmetric stereo-configurations (Fig. 1B). From a side view, the central [3]radialene ring and the exocyclic double bonds in **TTRO** maintain a near coplanar conformation (Fig. 1B), with dihedral angles of less than 15° between the central ring and the side wings. It should be noted that the three sulfone-xanthene side wings do not constitute the typical propeller conformation seen in many aromatics, where ~90° dihedral angles are formed.[35] Interestingly, two of the wings (A/B and E/F) have a twisted-folded conformation oriented in the in-plane direction, while the other ring (C/D) is oriented in the opposite direction (Fig. 1B). For example, the crystalline **Hex@TTRO** has the aryl group on the thioxanthene ring that rotates non-oriented around the central [3]radialene, forming a pair of (*P, M, M*) and (*M, P, P*) enantiomers (Fig. S8).This feature is likely due to the stabilization of the planarization and aromatization of the radialene system, which is modulated by the steric and electron-deficient effects of the sulfone group.[27]

These crystalline structures exhibit large stereochemical variations and asymmetries (*e.g.* bond lengths and dihedral angles), suggesting dynamic molecular flexibility in the solid state (Fig. 1B, Tables S5 and S6). In these single-crystal structures, the three-member rings of the [3]radialene are all non-equilateral triangles with different bond lengths (Table S6). Regardless of the presence of solvent molecules, the dihedral angles of the C and D benzene rings of the four **TTRO** crystalline molecules are ~44°, and the C_2=C_6 bond lengths are close to normal alkenes (1.350 Å) (Tables S5–S6). In the **Non@TTRO** crystalline framework without guest solvents, the dihedral angle between the two benzene rings (A and B) is 13.9°, indicating a nearly coplanar conformation. The corresponding connected exocyclic C_1=C_4 bond is 1.372 Å (Fig. 1B and Table S6), which is significantly longer than the normal alkene bond length (1.350 Å). This elongation is likely to be associated with decreased distortion between neighboring thioxanthene groups. In the crystalline framework with guest solvent molecules, the dihedral angles between the A and B rings increased to 25.5°, 26.2°, and 35.9°, for **THF@TTRO**, **Hex@TTRO**, and **DMF/MeOH@TTRO** crystals, respectively. Meanwhile, the corresponding C_1=C_4 bonds are notably relaxed to 1.361 Å, 1.363 Å, and 1.357 Å, respectively (Fig. 1B and Table S6). Similarly, the dihedral angle between the E and F rings in **Non@TTRO** is 38.4°, with the C_3=C_5 bond elongating to 1.357 Å. In the presence of solvent in the framework, the planes of E and F rings become more stereospecific, forming a dihedral angle of ~50°, and the exocyclic C_3=C_5 is compressed to 1.346 Å, 1.339 Å and 1.341 Å for **Hex@TTRO**, **THF@TTRO** and **DMF/MeOH@TTRO**, respectively. The exact parameters of the three thioxanthene rings differ from each other, showing asymmetric stereo-configurations in the framework state (Fig. 1B, Tables S5 and S6).

Supramolecular stacking and diverse porosity

These crystals show interesting and quite distinguishable three-dimensional stacking structures. **TTRO** crystals without solvent inclusion belong to the monoclinic crystal system with the $P2_1/n$ space group (Table S1). When guest molecules such as nonpolar *n*-hexanes or polar THF are present, these crystalline frameworks show similar unit cell parameters and are still monoclinic, but with different space groups: $P12_1/c1$ for **Hex@TTRO** (Table S2) and $P2_1/c$ for **THF@TTRO** (Table S3). When polar DMF/MeOH molecules are present, the resulting crystalline framework is triclinic, belonging to the *P*-1 space group (Table S4).

We next examine the crystalline molecular stacking arrangements to understand the assembly principle of the topological [3]radialene. As is shown, there are four **TTRO** molecules in the **Non@TTRO** unit cell, forming two pairs of (*P, M, M*) and (*M, P, P*) isomers (Fig. 2A and S9). The packing of individual **TTRO** molecules gives rise to a columnar structure, which subsequently forms an S-shaped layered structure along the *c*-axis direction (Fig. 2B). These layers are closely packed, which is responsible for the near planarity of one of the thioxanthene rings within the **TTRO** molecule in the crystalline structure (Fig. 1B). Calculations performed by Planton revealed that **Non@TTRO** has a porosity of 0% which was further confirmed by its spacefill mode (Fig. 2C). In **Hex@TTRO** crystals, **TTRO** molecules are aligned linearly in one direction *via* π–π interactions (d = 3.37 Å) between thioanthracene fragments. They then extend in parallel *via* C–H···O bonding interactions (d = 2.52 Å) to form a two-dimensional lamellar arrangement (Fig. 2D). Adjacent lamellar layers are intercalated with a large void space containing guest molecules, forming a special 3D hydrogen-bonded organic framework with continuous tunnels (Fig. 2E). When the crystal is rotated horizontally, microscale pores of different sizes can be observed along the vertical *c*-axis. These tunnels are regularly arranged, alternating with minimal intersection dimensions of 2.8 × 4.1 Å and 4.7 × 7.9 Å in the *b*-axis direction (Fig. 2F), and 8.9 × 7.8 Å along the *a*-axis (Fig. S10). As is shown, these tunnels in different directions within one plane are interconnected to form a continuous void network. The internal surface of these porous structures between layers is rich in polar sulfonyl arrays and is likely stabilized by supramolecular interactions with guest molecules in the middle which indicates its non-permanent porosity (Fig. S11). The accessible void volume of **Hex@TTRO** crystals was calculated to be 31.2% by Planton following the removal of guest solvent molecules (Fig. 2D–F). The N_2 gas adsorption isotherm of the polycrystalline **Hex@TTRO** solids revealed a Brunauer–Emmett–Teller surface area of 4.9 $m^2\ g^{-1}$, and a maximum N_2 uptake of 65.0 $cm^3\ g^{-1}$ at 77 K (Fig. S12 and S13). The self-assembled frameworks are characterised by asymmetric connectivity and a distribution of diverse pore apertures, created using sulfone-[3]radialene building blocks. These features make them quite unique and rare among organic porous materials.[36–43]

The overall stacking structure of **THF@TTRO** is like that of **Hex@TTRO**; however, no π–π interaction pattern was observed to guide the self-assembly process (Fig. 2G). Instead, including THF-mediated C–H···O interactions with sulfonyl groups (d = 2.71 Å, 2.49 Å and 2.70 Å) bridged the molecules within and between the unit cells, forming continuous 2D laminar layers (Fig. 2H). Only isolated tunnels were observed along the *c*-axis

direction in the framework, with minimal intersection dimensions of 6.0 Å × 4.5 Å (Fig. 2I). The solvent-accessible void spaces were calculated to be 21% after removal of the guest molecules (Fig. 2I). The crystalline layer-to-layer structures regularly host solvent molecules between the laminar layers (Fig. 2G). Therefore, the **THF@TTRO** framework is a cooperative self-assembly of THF and **TTRO** molecules. The loss of THF molecules results in an extremely low material stability, making the framework highly susceptible to weathering and fragmentation in air.

The **DMF/MeOH@TTRO** framework differed significantly from the other two described above. The unit cell contains two **TTRO** molecules arranged in a reverse, parallel, head-to-tail orientation (Fig. 2J). These molecules primarily engage in face-to-face π–π interactions ($d = 3.25$ Å), with two phenyl rings from two thioanthracene wings almost in overlap (Fig. 2J and S14A). Additionally, multiple C–H···O interactions occur between the sulfonyl group of one thioxanthene ring and a neighbouring benzene ring hydrogen (Fig. S14B). The **TTRO** molecules in the unit cell are stacked along the *a*-axis to create a columnar structure. These cell units are arranged repetitively and can be stacked to form a microporous channel with a cross-sectional diameter of ~9.0 × 10.6 Å (Fig. 2K and L). Unlike the **Hex@TTRO** crystals, these pores are mutually independent and penetrable, with a porosity of 21.8%. The versatile framework materials based on sulfone[3]radialene **TTRO** demonstrate the potential application of [3]radialene derivatives as organic building blocks for constructing topological framework materials.[44]

Surface analysis of interconnected pores

To gain insights into the surface properties within **TTRO** frameworks, Hirshfeld surface analysis was performed (Fig. 3, S15 and S16).[45–48] In the maps, red surfaces indicate strong interactions, where the distances between molecules are shorter than the sum of their van der Waals radii. Conversely, white and blue surfaces denote weak interactions, with contacts that are approximately equal to or longer than the van der Waals radii. Fig. 3 clearly shows strong interactions between adjacent molecules in the red regions around the sulfone groups. Additionally, π–π stacking interactions between aromatic rings can be observed in certain molecular pairs, contributing to the stability of the crystal structure. Specifically, C···C contacts contribute the least (~6%) to the total Hirshfeld surface (**Hex@TTRO**, Fig. 3A; **DMF/MeOH@TTRO**, Fig. 3B), indicating weak π–π stacking between adjacent molecules. In these crystals, H···O interactions contribute 35~37% to the total Hirshfeld surface. These significant contributions emphasize the vital role of the sulfone group in forming these framework materials.

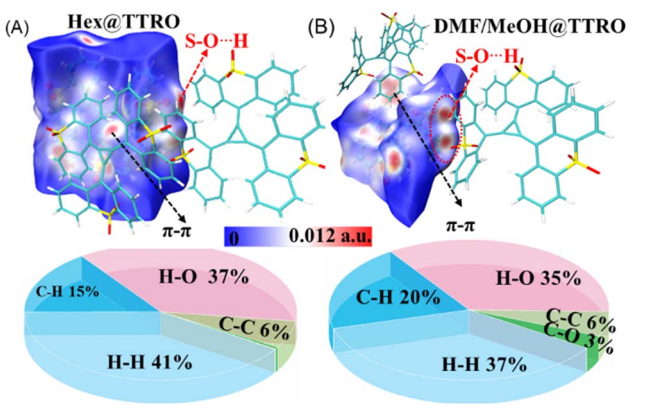

Fig. 3 Hirshfeld surface analysis (top) and relative contributions of the intermolecular interactions to the Hirshfeld surface area (down) of (A) Hex@TTRO and (B) DMF/MeOH@TTRO frameworks.

State-dependent optical properties revealing the critical CIE phenomenon

The photophysical properties of **TTRO** molecules in different physical states, as well as four different **TTRO** crystalline forms, were characterized and exhibited a critical crystalline-induced emission (**CIE**) phenomenon (Fig. 4). **TTRO** absorption in the solution state is primarily concentrated in the 390–690 nm range, with a maximum at 529 nm (Fig. 4A and S17). This corresponds to a molar extinction coefficient of $\varepsilon = 1.9 \times 10^4$ M^{-1} cm^{-1}, resulting in a violet color. Compared to the maximum absorption of **TTR** at 600 nm,[34] the blue-shifted maximum absorption of **TTRO** is consistent with the theoretical calculation results for the enhanced bandgap ($E_g = 2.07$ eV) of **TTRO** compared to **TTR** ($E_g = 1.88$ eV) (Fig. S18). Amorphous **TTRO** powder and crystals exhibit broad absorption in the 250–750 nm range without fine peaks (Fig. 4A). Notably, brownish-red **Hex@TTRO** crystals were ground to produce a brownish-black powder. Despite their apparent different colours and appearances, their solid-state absorption spectra are almost identical, except for the powder state's wider absorption range of 430–710 nm compared to the crystal state.

Interestingly, neither the **TTRO** solution nor the amorphous powder is fluorescent, with a PLQY of less than 0.1% (Fig. 4B). However, the **Hex@TTRO** crystals exhibit strong fluorescence in the deep red region (λ_{em} = 695 nm) when excited at λ_{ex} = 408 nm (Fig. 4B and S19). The photoluminescence spectrum extends to the near-infrared II region at 1100 nm with a PLQY of 16.1% (Fig. 4B and Table S7). Clearly, the photoluminescence of **TTRO** is highly dependent on its physical state, with crystallization accompanied by a dramatic change in fluorescence from off to on, indicating a stringent and critical **CIE** phenomenon.[49–51]

The **TTRO** crystals exhibit tunable NIR luminescence depending on the molecular packing structure (Fig. 4C–F). Similar to **Hex@TTRO** ($\lambda_{ex}/\lambda_{em}$ = 408/695 nm, PLQY = 16.1%), **THF@TTRO** ($\lambda_{ex}/\lambda_{em}$ = 395/706 nm, PLQY = 14.6%, Fig. 4D) and **DMF/MeOH@TTRO** ($\lambda_{ex}/\lambda_{em}$ = 380/698 nm, PLQY = 24.1%, Fig. 4E) both exhibited dramatically enhanced emission in the deep-red/NIR region with a large Stokes shift of ~285 nm. To be noted, the **Non@TTRO** crystalline solids without guest solvent fluoresced weakly ($\lambda_{ex}/\lambda_{em}$ = 375/685 nm, PLQY < 0.1%, Fig. 4F), possibly due to excited-state exciton annihilation resulting from tight packing *via* π–π interactions (Fig. S20). Time-resolved fluorescence decay studies revealed that the fluorescence decay lifetime of **DMF/MeOH@TTRO** crystals is estimated to be

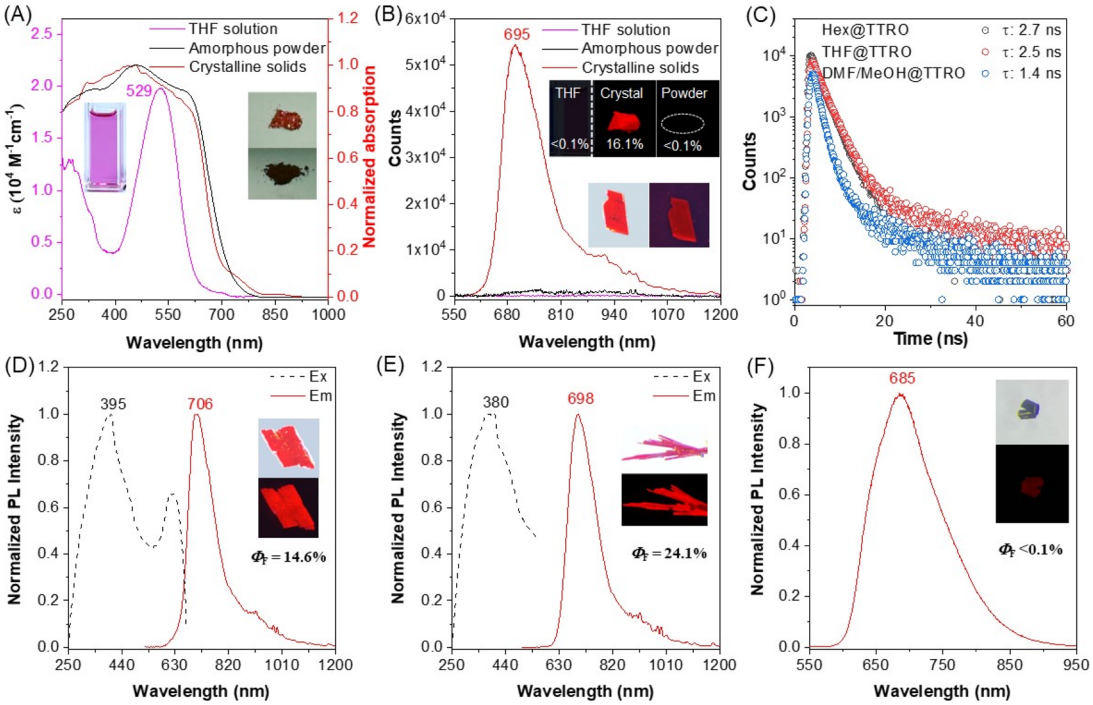

Fig. 4 Photophysical properties of TTRO materials dissolved in THF solution, as amorphous powder and crystalline frameworks. (A) UV-Vis-NIR absorption spectra. Crystal sample: **Hex@TTRO**. (B) PL emission spectra. Concentration: 1×10^{-5} M. Crystal sample: **Hex@TTRO**. (C) PL decay curves of three different crystal samples. (D, E and F) PL spectra of **THF@TTRO** (D), **DMF/MeOH@TTRO** (E) and **Non@TTRO** crystalline solids (F).

1.4 ns. In contrast, the lifetimes of **Hex@TTRO** and **THF@TTRO** are much longer, at 2.7 ns and 2.5 ns, respectively (Fig. 4C and Table S7). Fitting analysis shows that the radiative rate of **DMF/MeOH@TTRO** ($k_r = 1.72 \times 10^8$) is almost three times larger than that of the other samples ($k_r = 0.6 \times 10^8$), even though the non-radiative rate ($k_{nr} = 5.42 \times 10^8$) has also increased slightly compared to the other crystalline samples ($k_{nr} = 3.42 \times 10^8$). The increased fluorescence efficiency in **DMF/MeOH@TTRO** is therefore attributed to the significantly higher radiative rates.

Relationships between molecular packing and solid-state fluorescence

The similar excitation/emission spectra, coupled with varied fluorescence efficiency, suggest an intricate fluorescence scenario in the crystalline state of these **TTRO** frameworks. This is likely tuned by the interplay of intermolecular interactions and the specific electronic structure of the [3]radialene fluorophore.[4,51] DFT-based computational analysis of different crystalline structures yielded almost close energy levels, which are consistent with the excitation/emission characteristics (Fig. 5, left). The highest occupied molecular orbitals (HOMOs) in these **TTROs** are predominantly located on the central radialene ring but are also extended across all three oxidized thioxanthene wings *via* exocyclic double bonds. Notably, the bottom two wings of the **TTRO** in all these porous frameworks are more widely spaced in the HOMO/LUMO plots than the **Non@TTRO** (by arrows, Fig. 5). This suggests that these molecular systems resonantly conjugate as a whole when they are photo-excited. The asymmetrical electronic structure can be revealed further in three-dimensional electrostatic surface potential (ESP) analysis, which shows distinct changes in dipole moments in different molecular stereo-configurations (Fig. 5, right). The red, electronic-deficient region is predominantly located on the periphery of the three sulfonyl groups, while the central radialene ring and phenyl rings are relatively electron-rich and appear blue. In **Non@TTRO** crystals without guest solvents, the

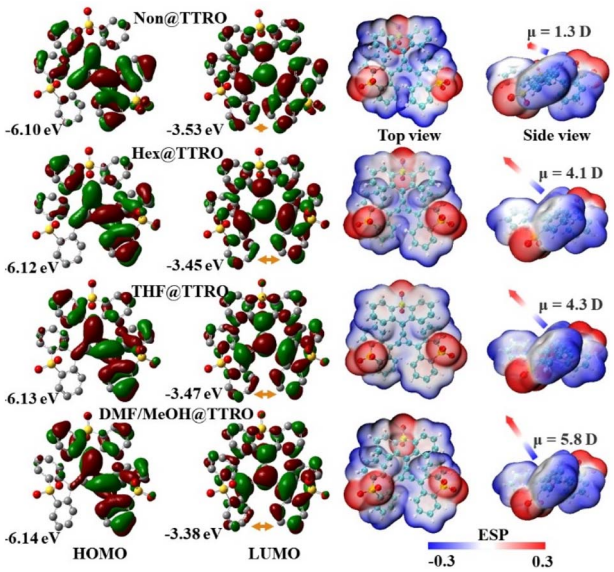

Fig. 5 HOMO and LUMO amplitude plots (left) and the Electrostatic Potential Surface (ESP) image (right), calculated at the B3LYP/6-31G(d,p) level based on single crystal structures.

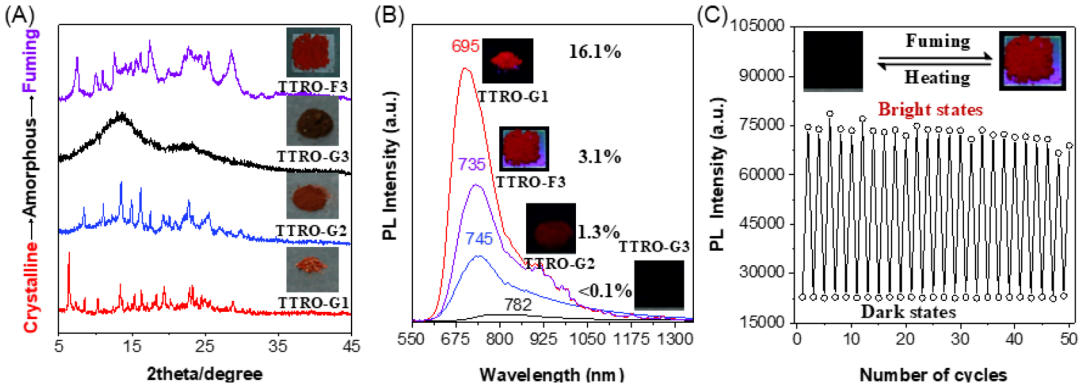

Fig. 6 (A) XRD patterns of TTRO samples with different levels of crystallinity, obtained through grinding and fuming. (B) Corresponding photoluminescence emission spectra (λ_{ex} = 473 nm). (C) Reversible heating and fuming process for the TTRO sample.

TTRO molecule has a dipole moment of 1.3 Debye, oriented at a small angle to the central radialene plane, resulting in a planar skeleton conformation. In the **Hex@TTRO** and **THF@TTRO** frameworks containing guest solvents, the **TTRO** molecules exhibit much increased dipole moments of 4.1–4.3 Debye, with an increased, but similar vector direction angle to the central ring (Fig. 5). When polar solvent molecules are present as guests, the **TTRO** molecule in the **DMF/MeOH@TTRO** further exhibits significant dipole moments of 5.8 Debye, with the overall dipole vector being almost perpendicular to the central radialene. Following the direction of the dipole moments' vectors, these molecules stack with each other in line columns and form a stable porous framework with mutually independent pores and tight electronic communication within the crystal (Fig. 2). Furthermore, the charge density difference maps visually manifest the effect of dipole moment variation on the electronic interactions in the crystalline state. In **DMF/MeOH@TTRO**, there are stronger π–π interactions (3.25 Å) between **TTRO** molecules (Fig. S22A). Consequently, electron transfer and accumulation are more pronounced at the π–π interaction sites, whereas these effects are relatively weaker along the hydrogen-bonding direction (Fig. S22C). This charge redistribution corresponds to the larger dipole moment of **TTRO** in the **DMF/MeOH@TTRO** crystal. In **Hex@TTRO**, electron transfer and accumulation in the π–π interaction region (3.37 Å) are weaker and substantial redistribution also occurs in the weaker S–O···H interaction regions (Fig. S22B and D), resulting in less extensive charge redistribution. This observation is consistent with the smaller dipole moment of **Hex@TTRO**.

To understand the critical crystalline-induced photoluminescence, we investigate the correlation between different levels of crystallinity and luminescent properties during mechanical grinding, reverse fuming, and heating treatments. The pristine **TTRO-G1** exhibited sharp XRD peaks, indicating perfect crystallinity (Fig. 6A). After gentle grinding, the sharp peaks decreased and a new set of peaks appeared in the 2θ range of 20°–30° (**TTRO-G2**, Fig. 6A). Continuous grinding produced broad peaks, indicating an amorphous state (**TTRO-G3**, Fig. 6A). Reduced crystallinity resulted in red-shift luminescence and a dramatic decrease in luminescence efficiency when compared to **TTRO-G1** (λ_{em} = 695 nm, PLQY = 16.1%). Specifically, **TTRO-G2** exhibited a maximum emission wavelength (λ_{em}) of 745 nm with a PLQY of 1.3%, while **TTRO-G3** displayed a λ_{em} of 782 nm and a PLQY of <0.1%. This demonstrates the highly state-dependent nature of photoluminescence of **TTRO** (Fig. 6B). The blue-shifted photoluminescence of the crystalline state compared to the amorphous powder is primarily attributed to strained and distorted molecular conformations in the crystalline state. This is a typical feature of **CIE**-active molecules.[49] Interestingly, after being fumed with solvents for several minutes, the amorphous powder underwent a reverse colour change, shifting from brownish black (**TTRO-G3**) to dark red (**TTRO-F3**). Meanwhile, the corresponding XRD spectra became clearer and sharper, showing new peaks in the 2θ range of 5°–30°. This suggests a reversible recrystallisation process involving solvent fuming. When subjected to thermal heating at 75 °C for a period, the dark red, luminescent, chloroform-fumed **TTRO-F3** (λ_{em} = 735 nm, PLQY = 3.1%) exhibited a rapid colour change to brownish black, accompanied by a loss of photoluminescence (Fig. 6B and Table S8). Upon cooling to room temperature and re-exposure to chloroform fumigation, the material returned to its original dark red colour with comparable photoluminescence (Fig. 6C). This process

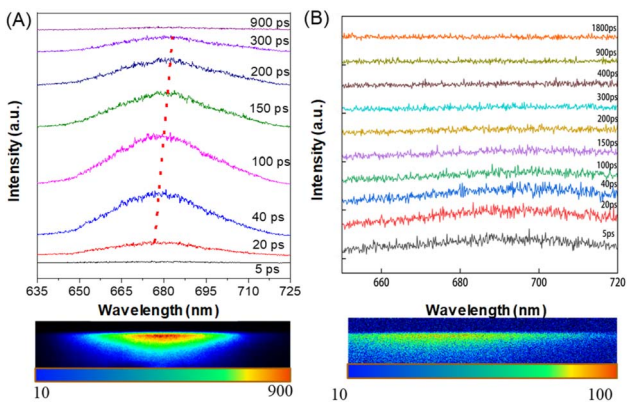

Fig. 7 Picosecond time-resolved PL spectra of (A) crystalline Hex@TTRO and (B) amorphous TTRO.

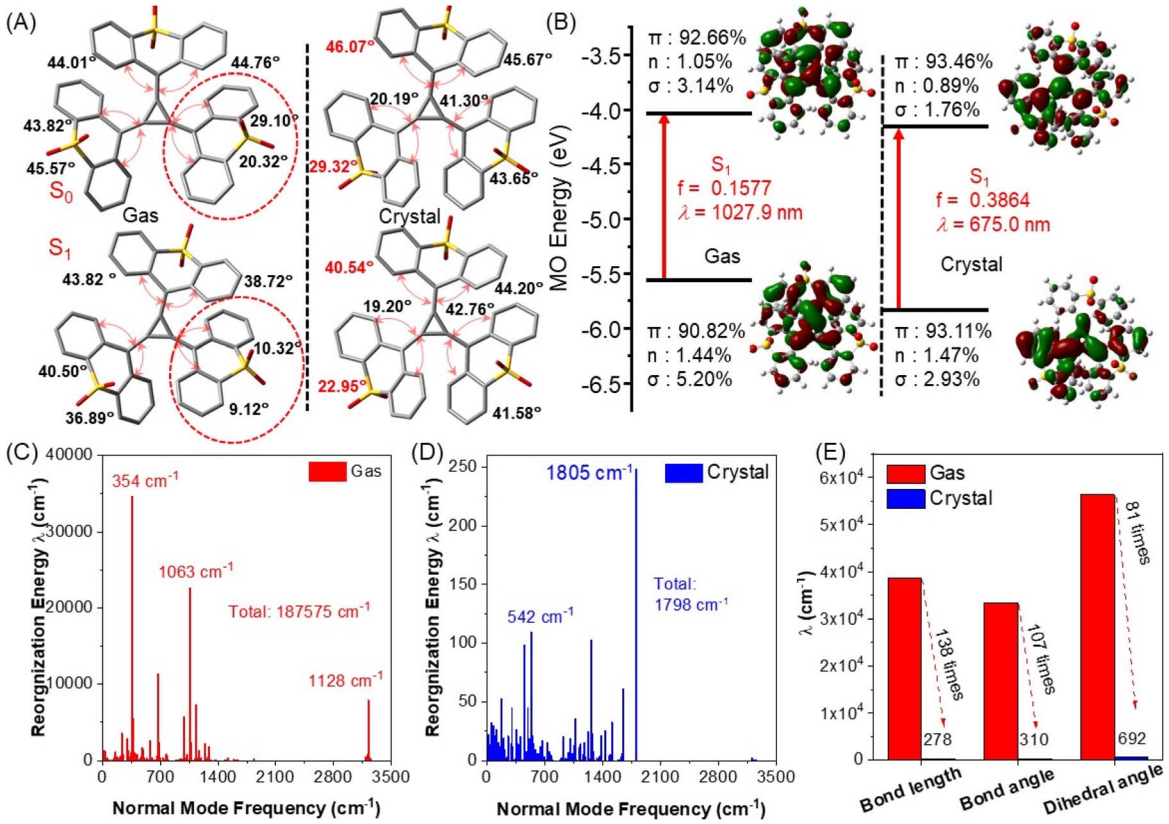

Fig. 8 Computational results of isolated TTRO and crystalline TTRO (Hex@TTRO). (A) Optimized geometries at ground and excited states, showing dihedral angles between the benzene ring and the [3]radialene skeleton. (B) Involved molecular orbital levels in electronic transitions, energy levels, transition components and oscillator strengths at the S_1 state. (C) Reorganization energy in the gas state. (D) Reorganization energy in the crystalline state. (E) Variations in bond length, bond angle and dihedral angle contribution to reorganization energy in both the gas and crystalline states.

demonstrated good reversibility, as shown by ~50 cycles of repeated fuming and heating tests. The optical properties of **TTRO** are highly sensitive to the packing of the molecules. The excellent reversibility and operational reproducibility of these frameworks suggest that they are promising candidates for dual-mode information storage materials.

Ultrafast time-resolved fluorescence spectroscopy study

Given the intriguing phenomenon that crystalline frameworks exhibit luminescence whereas their amorphous powders do not, we aim to investigate the dynamic process of stringent changes in optical behavior using ultrafast time-resolved fluorescence spectroscopy. Fig. 7 shows the picosecond time-resolved fluorescence spectra of **TTRO** crystals and powders following excitation. Excitation by a 400 nm laser resulted in the photoluminescence of the crystalline **Hex@TTRO** frameworks, which fluoresced with a single sharp peak exhibiting a full width at half maximum (FWHM) of ~30 nm. This peak quickly red-shifted from ~672 nm during the initial 20 ps period to ~683 nm after 200 ps (Fig. 7A). Emission intensity increased within the first 100 ps; after this, it decreased within the subsequent 100–300 ps period and disappeared completely after 900 ps. The amorphous powder sample displayed only weak fluorescence at ~685 nm within the initial 20–40 ps and gave no fluorescence signal beyond 100 ps (Fig. 7B and S21). This suggests that, upon photoexcitation, the energy of the **TTRO**'s excited state is quickly dissipated through non-radiative decay within the first 100 ps in the amorphous powder.

In comparison to the relatively loose amorphous samples, which exhibit enhanced flexibility and only emit weak fluorescence at 685 nm within the first 40 ps, the crystalline framework showed a gradual red shift in luminescence wavelength from 672 nm to 683 nm as the relaxation time increased. We speculate that the sulfone-functionalized **CIE** molecules in these organic porous frameworks are likely to be in a similarly flexible environment, characterized by the dynamic motions of **TTRO** and rich non-covalent intermolecular interactions. These endow the **TTRO** emitters with certain movement in the excited state, leading to partial relaxation of the excited state and thus longer emission wavelengths. Nevertheless, the relatively small red shift indicates the high rigidity of the porous framework, which exhibits notable fluorescence efficiency in its crystalline state.

Mechanistic investigation of the CIE phenomenon

As the above experiments suggested, the rich intermolecular interactions (**TTRO**–**TTRO** and **TTRO**-solvent) within crystalline frameworks are likely to modulate the dynamic processes of excited-state emitters, effectively attenuating the coupling

between the electrons and molecular vibrations. This induces photoluminescent adaptability at the molecular aggregate level. In this regard, quantum theory calculations were performed to gain an intuitive understanding of the unique **CIE** phenomenon whereby crystallization triggers the luminescence of **TTRO** sulfone[3]radialene. The molecular aggregation effect was considered using the ONIOM method with QM and MM layers (Fig. S23). The ground-state molecular geometries of the crystalline and freely dissolved **TTRO** differ only slightly, with a slight change in the dihedral angle between the benzene ring and the [3]radialene. This suggests a similar absorption property in the dilute solution and the crystalline phase, which is consistent with the experimental phenomenon (Fig. S24 and Table S9). Following photon excitation, the **TTRO**'s geometric variations differ considerably in different microenvironments. In the gas and solution phases, almost all dihedral angles decrease from S_0 to S_1, particularly those of the oxidized thioxanthene (red), which easily unbend and become nearly coplanar in the S_1 state, decreasing to 10.32°/9.12° from 29.10°/20.32° in the S_0 state (Fig. 8A). In the crystalline phase, the **TTRO** molecules remain in a highly distorted configuration following excitation. Two of the labelled dihedral angles decrease by only ~7°, while the rest remain almost identical to the S_0 configuration. This weakens the molecular non-radiative rate in the impact crystal, making luminescence more favorable (Fig. 8A).

Furthermore, Natural Bond Orbital (NBO) analysis shows that the S_1 state involves a dipole-allowed π to π* orbital transition in both the solid and gas phases (Fig. 8B and Table S10).[47,48] Of these states, the lowest (S_1) in the crystalline state has an oscillator strength (*f*) of 0.3864 and a vertical excitation energy of 1.8368 eV. This corresponds to an estimated emission wavelength of $\lambda_{em} = 675$ nm, which is in close agreement with the experimental observation of $\lambda_{em} = 695$ nm. Meanwhile, the S_1 state in the gas phase is estimated to have an oscillator strength of $f = 0.1557$ and a vertical excitation energy of 1.2062 eV. This is much smaller than the value observed in the crystalline state ($f = 0.3864$). Accordingly, **TTRO** could exhibit photoluminescence at ~1028 nm in the gas phase. Unfortunately, however, we did not observe this phenomenon in our experimental measurements.

We also examined the non-radiative decay pathways of bright S_1 states in both the gas and crystal phases (Fig. 8C and D). The reorganization energy (λ) reflects the change in geometric configuration between two electronic states when a photon is absorbed or emitted. It also represents the degree of electron-vibrational coupling within a molecule. A smaller reorganization energy indicates a smaller change in molecular conformations before and after photon excitation. Specifically, the reorganization energy corresponding to each frequency in the normal mode represents the non-radiative decay process of the excited state due to intramolecular motions. Changes in the recombination energy in the low-frequency region (below 400 cm^{-1}) are positively correlated with intramolecular rotation, while changes in the high-frequency region are positively correlated with the telescopic vibrations of intramolecular bonds.[52] The total recombination energy of **TTRO** in the crystalline state is 1798 cm^{-1}(Fig. 8D), which is significantly lower than in the gas phase (187 575 cm^{-1}) (Fig. 8C). To elucidate the contributions of configurational parameter variations, we analyzed the correlations between specific structural changes (*e.g.* bond lengths, bond angles and dihedral angles) and the corresponding reorganization energy components (Fig. 8E). In the crystalline state, all structural deformations in the **TTRO** frameworks were significantly reduced, resulting in a substantial decrease in reorganization energy compared to the gas phase. The rigid environment of the crystalline state reduces the recombination energy effectively, thus weakening the non-radiative decay rate and triggering fluorescence. The variation in the reorganization energy of **TTRO** in the gas state primarily occurs in the relatively low-frequency region. Reorganization energy reaches approximately 35 000 cm^{-1} at the normal mode frequency of 354 cm^{-1}, whereas higher-frequency vibrations at 1063 cm^{-1} exhibit a lower value of ~23 000 cm^{-1} (Fig. 8C). In contrast, the reorganization energy in the low-frequency region of the crystalline state remains exceptionally low at less than 50 cm^{-1} (Fig. 8D). Following photoexcitation, low-frequency vibrational modes tend to undergo mutual mixing, thereby activating multiple non-radiative decay pathways. This phenomenon, known as the Duschinsky rotation effect (DRE),[53] significantly increases the rate of non-radiative decay and serves as the primary mechanism responsible for the absence of luminescence in **TTRO** compounds, whether in solution or in an amorphous powder state.

Conclusions

We present a special class of dynamic framework materials based on a sulfone-functionalized stereoisomeric [3]radialene **TTRO**. The **TTRO** synthesis is based on an optimized Fukunaga condensation protocol and involves efficient sulfide oxidation. The resulting **TTRO** exhibits flexible stereo-configurations with quasi-C_3 symmetry and can form diverse crystalline frameworks in various chemical environments. These frameworks have variable 3D packing structures and porosities ranging from 0% to 31.2%. **TTRO**-based organic frameworks exhibit a critical crystallization-induced NIR emission phenomenon: they are not emissive in solution or as amorphous powders but become emissive in guest-involved crystalline frameworks. The exact stacking structure can be adjusted to control the corresponding solid-state emission properties, which are influenced by the guest solvent molecules. Specifically, the luminescence wavelengths of these frameworks range from 685 to 710 nm, but their luminescence efficiencies vary considerably. The **Non@TTRO** crystals have tight stacking (porosity: 0%, PLQY: <0.1%), whereas the **DMF/MeOH@TTRO** crystalline frameworks have independently penetrating pores (porosity: 21.8%, PLQY: 24.1%), and the **Hex@TTRO** crystalline frameworks have two-dimensional interconnected pores (porosity: 31.2%, PLQY: 16.1%). Solid-state superstructure analysis and theoretical calculations demonstrate that multivalent intermolecular interactions involving sulfone groups are essential for constructing these diverse framework materials. The reorganization energy between the ground and excited states is reduced by

99% in the solid phase compared to the gas phase. This reduction is essential for initiating crystalline-induced luminescence emission. This observation highlights the presence of active molecular motions in the solid state of these flexible [3] radialene units, which are greatly suppressed in the porous frameworks containing guest molecules, leading to significantly higher luminescence efficiency in the crystalline state. These sulfone-functionalized **TTRO**-based frameworks demonstrate modifiable supramolecular porous structures featuring both luminescence and absorption functionalization. This establishes a scientific foundation for the development of radialene-based materials for use in sensing and solid-state optics.

Author contributions

G. Q. Xu: methodology, data curation, investigation, writing – original draft. Y. Zhao, Z. B. Zhou: data curation, investigation. Z. Y. Luo, H. H. Liu, Y. Zhang and Z. Q. Qiu: data curation, software, resources. S. Xie: conceptualization, funding acquisition, writing – review & editing. A. L. Pan, Z. B. Zeng: resources, supervision, writing – review & editing. B. Z. Tang: funding acquisition, writing – review & editing, conceptualization.

Conflicts of interest

There are no conflicts to declare.

Data availability

CCDC 2476303 (**DMF/MeOH@TTRO**), 2476304 (**Non@TTRO**), 2476305 (**Hex@TTRO**) and 2476306 (**THF@TTRO**) contain the supplementary crystallographic data for this paper.[54a–d]

The data supporting this article have been included as part of the Supplementary Information (SI). Supplementary information: all synthetic protocols, spectroscopic data, SI figures and tables. See DOI: https://doi.org/10.1039/d5sc06925d.

Acknowledgements

This work was supported by the National Natural Science Foundation of China (T2122011), Natural Science Foundation of Hunan Province (2023JJ50002), Shenzhen Science and Technology Program (JCYJ20220530160403008), Guangdong Basic and Applied Basic Foundation (2025A1515011016), National Key Research and Development Program of China (2023YFB3810001), National Natural Science Foundation of China (52333007), Key-Area Research and Development Program of Guangdong Province (2024B0101040001), Shenzhen Key Laboratory of Functional Aggregate Materials (ZDSYS20211021111400001), and the Science Technology Innovation Commission of Shenzhen Municipality (KQTD20210811090142053). Thanks to the Analytical Instrumentation Centre of Hunan University, and the AIE Institute (www.aietech.org.cn) for providing technical assistance.

References

1 H. Hopf and M. S. Sherburn, *Cross Conjugation: Modern Dendralene, Radialene and Fulvene Chemistry*, John Wiley & Sons, 2016.
2 M. Gholami and R. R. Tykwinski, *Chem. Rev.*, 2006, **106**, 4997–5027.
3 E. A. Dorko, *J. Am. Chem. Soc.*, 1965, **87**, 5518–5520.
4 C. Wright, J. Holmes, J. W. Nibler, K. Hedberg, J. D. White, L. Hedberg, A. Weber and T. A. Blake, *J. Phys. Chem. A*, 2013, **117**, 4035–4043.
5 D. Y. Li, Y. Wang, X. Y. Hou, Y. T. Ren, L. X. Kang, F. H. Xue, Y. C. Zhu, J. W. Liu, M. Liu and X. Q. Shi, *Angew. Chem., Int. Ed.*, 2022, **134**, e202117714.
6 G. Xu, H. Liu, Z. Zhou, W. Lai, B. Li, Y. Zhou, R. Hu, W. Yao, K. Yang, S. Xie and Z. Zeng, *Angew. Chem., Int. Ed.*, 2023, **62**, e202305011.
7 S. Charoughchi, J. T. Liu, M. Berteau-Rainville, H. Hase, M. S. Askari, S. Bhagat, P. Forgione and I. Salzmann, *Angew. Chem., Int. Ed.*, 2023, **62**, e202304964.
8 F. Hasan, J. H. Gillen, A. T. Jayaweera, W. D. McDearmon Jr, A. H. Winter and C. M. Bejger, *Chem. Eur. J.*, 2024, **30**, e202302829.
9 B. K. Hillier, D. M. de Clercq, S. D. S. Bortolussi, S. S. Capomolla, M. P. Nielsen, K. Mlodzikowska-Pienko, R. Gershoni-Poranne, T. W. Schmidt and M. D. Peeks, *Chem. Sci.*, 2025, **16**, 11331–11338.
10 H. Hopf, *Angew. Chem., Int. Ed.*, 2012, **51**, 11945–11947.
11 H. Hopf and G. Maas, *Angew. Chem., Int. Ed.*, 1992, **31**, 931–954.
12 Y. Karpov, T. Erdmann, I. Raguzin, M. Al-Hussein, M. Binner, U. Lappan, M. Stamm, K. L. Gerasimov, T. Beryozkina, V. Bakulev, D. V. Anokhin, D. A. Ivanov, F. Gunther, S. Gemming, G. Seifert, B. Voit, R. Di Pietro and A. Kiriy, *Adv. Mater.*, 2016, **28**, 6003–6010.
13 J. Saska, G. Gonel, Z. I. Bedolla-Valdez, S. D. Aronow, N. E. Shevchenko, A. S. Dudnik, A. J. Moulé and M. Mascal, *Chem. Mater.*, 2019, **31**, 1500–1506.
14 Y. Liu, B. Nell, K. Ortstein, Z. Wu, Y. Karpov, T. Beryozkina, S. Lenk, A. Kiriy, K. Leo and S. Reineke, *ACS Appl. Mater. Interfaces*, 2019, **11**, 11660–11666.
15 J. Saska, N. E. Shevchenko, G. Gonel, Z. I. Bedolla-Valdez, R. M. Talbot, A. J. Moulé and M. Mascal, *J. Mater. Chem. C*, 2021, **9**, 15990–15997.
16 J. L. Benham, R. West and J. A. T. Norman, *J. Am. Chem. Soc.*, 1980, **102**, 5047–5053.
17 J. D. Evans, C. A. Hollis, S. Hack, A. S. Gentleman, P. Hoffmann, M. A. Buntine and C. J. Sumby, *J. Phys. Chem. A*, 2012, **116**, 8001–8007.
18 J. P. Soyka, J. F. Witte, A. Wiesner, A. R. Krappe, D. Wehner, N. Alnicola, B. Paulus, U. Resch-Genger and S. Eigler, *Eur. J. Org Chem.*, 2025, **28**, e20250066.
19 M. Iyoda, N. Nakamura, M. Todaka, S. Ohtsu, K. Hara, Y. Kuwatani, M. Yoshida, H. Matsuyama, M. Sugita, H. Tachibana and H. Inoue, *Tetrahedron Lett.*, 2000, **41**, 7059–7064.

20 T. Enomoto, N. Nishigaki, H. Kurata, T. Kawase and M. Oda, *B. Chem. Soc. Jpn.*, 2000, **73**, 2109–2114.
21 K. Matsumoto, N. Yamada, T. Enomoto, H. Kurata, T. Kawase and M. Oda, *Chem. Lett.*, 2011, **40**, 1033–1035.
22 K. An, Q. Qiao, L. Lovelesh, S. A. A. Abedi, X. Liu and Z. Xu, *Chin. Chem.Lett.*, 2025, **36**, 109786–109791.
23 C. A. Hollis, L. R. Hanton, J. C. Morris and C. J. Sumby, Design, *Cryst. Growth Des.*, 2009, **9**, 2911–2916.
24 K. Matsumoto, Y. Harada, T. Kawase and M. Oda, *Chem. Commun.*, 2002, **4**, 324–325.
25 P. J. Steel and C. J. Sumby, *Chem. Commun.*, 2002, **4**, 322–323.
26 K. Matsumoto, Y. Harada, N. Yamada, H. Kurata, T. Kawase and M. Oda, *Cryst. Growth Des.*, 2006, **6**, 1083–1085.
27 S. Tian, H. Ma, X. Wang, A. Lv, H. Shi, Y. Geng, J. Li, F. Liang, Z. M. Su, Z. An and W. Huang, *Angew. Chem., Int. Ed.*, 2019, **58**, 6645–6649.
28 S. Jiang, Y. Yu, D. Li, Z. Chen, Y. He, M. Li, G. X. Yang, W. Qiu, Z. Yang, Y. Gan, J. Lin, Y. Ma and S. J. Su, *Angew. Chem., Int. Ed.*, 2023, **62**, e202218892.
29 S. Jiang and S. J. Su, *ChemPhotoChem*, 2023, **8**, e202300197.
30 L. Zhan, Y. Xu, T. Chen, Y. Tang, C. Zhong, Q. Lin, C. Yang and S. Gong, *Aggregate*, 2024, **5**, e485.
31 K. Harrington, D. T. Hogan, T. C. Sutherland and K. Stamplecoskie, *Phys. Chem. Chem. Phys.*, 2023, **25**, 24829–24837.
32 T. Fukunaga, M. D. Gordon and P. J. Krusic, *J. Am. Chem. Soc.*, 1976, **98**, 611–613.
33 T. Enomoto, T. Kawase, H. Kurata and M. Oda, *Tetrahedron Lett.*, 1997, **38**, 2693–2696.
34 T. Sugimoto, Y. Misaki, T. Kajita, T. Nagatomi, Z. Yoshida and J. Yamauchi, *Angew. Chem., Int. Ed.*, 1988, **27**, 1078–1080.
35 B. P. Corbet, M. B. S. Wonink and B. L. Feringa, *Chem. Commun.*, 2021, **57**, 7665–7668.
36 X. Song, Y. Wang, C. Wang, D. Wang, G. Zhuang, K. O. Kirlikovali, P. Li and O. K. Farha, *J. Am. Chem. Soc.*, 2022, **144**, 10663–10687.
37 H. Liu, S. Wang, M. Huang, Q. Bian, Y. Zhang, K. Yang, B. Li, W. Yao, Y. Zhou, S. Xie, B. Z. Tang and Z. Zeng, *Small*, 2024, **20**, e2306956.
38 J. Xiao, A. R. M. Shaheer, C. Liu, T. F. Liu and R. Cao, *Aggregate*, 2024, **5**, e481.
39 J. Y. Zeng, X. S. Wang, Y. X. Sun and X. Z. Zhang, *Biomaterials*, 2022, **286**, 121583.
40 S. Dalapati, C. Gu and D. Jiang, *Small*, 2016, **12**, 6513–6527.
41 M. Asad, M. Imran Anwar, A. Abbas, A. Younas, S. Hussain, R. Gao, L.-K. Li, M. Shahid and S. Khan, *Coord. Chem. Rev.*, 2022, **463**, 214539–214565.
42 W. Liu, Q. Liu, D. Wang and B. Z. Tang, *ACS Nano*, 2024, **18**, 27206–27229.
43 Y. Zhang, S. Xie, Z. Zeng and B. Z. Tang, *Matter*, 2020, **3**, 1862–1892.
44 Z. Zhang, Y. Ye, S. Xiang and B. Chen, *Acc. Chem. Res.*, 2022, **55**, 3752–3766.
45 W. Humphrey, A. Dalke and K. Schulten, *J. Mol. Graph.*, 1996, **14**(33–38), 27–38.
46 M. A. Spackman and D. Jayatilaka, *Crystengcomm*, 2009, **11**, 19–32.
47 T. Lu, *J. Chem. Phys.*, 2024, **161**, 082503–082545.
48 T. Lu and F. Chen, *J. Comput. Chem.*, 2012, **33**, 580–592.
49 Z. Zhao, H. Zhang, J. W. Y. Lam and B. Z. Tang, *Angew. Chem., Int. Ed.*, 2020, **59**, 9888–9907.
50 Y. Dong, J. W. Lam, A. Qin, Z. Li, J. Sun, H. H. Sung, I. D. Williams and B. Z. Tang, *Chem. Commun.*, 2007, **1**, 40–42.
51 Y. Song, G. Pan, C. Zhang, C. Wang, B. Xu and W. Tian, *Mater. Chem. Front.*, 2023, **7**, 5104–5119.
52 S. Huang, J. Ding, A. Bi, K. Yu and W. Zeng, *Adv. Opt. Mater.*, 2021, **9**, 2100832–2100841.
53 G. M. Sando, K. G. Spears, J. T. Hupp and P. T. Ruhoff, *J. Phys. Chem. A*, 2001, **105**, 5317–5325.
54 (*a*) CCDC 2476304: Experimental Crystal Structure Determination, 2026, DOI: 10.5517/ccdc.csd.cc2p3ssd.; (*b*) CCDC 2476305: Experimental Crystal Structure Determination, 2026, DOI: 10.5517/ccdc.csd.cc2p3stf; (*c*) CCDC 2476306: Experimental Crystal Structure Determination, 2026, DOI: 10.5517/ccdc.csd.cc2p3svg; (*d*) CCDC 2476303: Experimental Crystal Structure Determination, 2026, DOI: 10.5517/ccdc.csd.cc2p3src.